Title

Kinetic analysis of multi-resolution hyperpolarized 13C human brain MRI to study cerebral metabolism

Journal

Magnetic Resonance in Medicine, 88(5)

ISSN

0740-3194

Authors

Hu, Jasmine Y

Kim, Yaewon

Autry, Adam W

et al.

Publication Date

2022-11-01

DOI

10.1002/mrm.29354

Peer reviewed

HHS Public Access

Author manuscript

Magn Reson Med. Author manuscript; available in PMC 2023 November 01.

Published in final edited form as:

Magn Reson Med. 2022 November ; 88(5): 2190–2197. doi:10.1002/mrm.29354.

Kinetic Analysis of Multi-Resolution Hyperpolarized ^{13}C Human Brain MRI to Study Cerebral Metabolism

Jasmine Y Hu[1,2], **Yaewon Kim**[1], **Adam W Autry**[1], **Mary M Frost**[1], **Robert A Bok**[1], **Javier E Villanueva-Meyer**[1], **Duan Xu**[1,2], **Yan Li**[1,2], **Peder EZ Larson**[1,2], **Daniel B Vigneron**[1,2], **Jeremy W Gordon**[1]

[1]Department of Radiology and Biomedical Imaging, University of California San Francisco, San Francisco, California

[2]UC Berkeley-UCSF Graduate Program in Bioengineering, University of California, San Francisco and University of California, Berkeley

Abstract

Purpose: To investigate multi-resolution hyperpolarized (HP) ^{13}C pyruvate MRI for measuring kinetic conversion rates in the human brain.

Methods: HP [1-^{13}C]pyruvate MRI was acquired in six subjects with a multi-resolution EPI sequence at 7.5 × 7.5 mm^2 resolution for pyruvate and 15 × 15 mm^2 resolution for lactate and bicarbonate. With the same lactate data, two quantitative maps of pyruvate-to-lactate conversion (k_{PL}) maps were generated: one using 7.5 × 7.5 mm^2 resolution pyruvate data and the other using synthetic 15 × 15 mm^2 resolution pyruvate data to simulate a standard constant resolution acquisition. To examine local k_{PL} values, four voxels were manually selected in each study representing brain tissue near arteries, brain tissue near veins, white matter, and gray matter.

Results: High resolution 7.5 × 7.5 mm^2 pyruvate images increased the spatial delineation of brain structures and decreased partial volume effects compared to coarser resolution 15 × 15 mm^2 pyruvate images. Voxels near arteries, veins and in white matter exhibited higher calculated k_{PL} for multi-resolution images.

Conclusion: Acquiring HP ^{13}C pyruvate metabolic data with a multi-resolution approach minimized partial volume effects from vascular pyruvate signals while maintaining the SNR of downstream metabolites. Higher resolution pyruvate images for kinetic fitting resulted in increased kinetic rate values, particularly around the superior sagittal sinus and cerebral arteries, by reducing extracellular pyruvate signal contributions from adjacent blood vessels. This HP ^{13}C study showed that acquiring pyruvate with finer resolution improved the quantification of kinetic rates throughout the human brain.

Keywords

Hyperpolarization; MRI; Kinetics; Carbon-13; Pyruvate

Corresponding Author: Jeremy Gordon, 1700 4th St, Byers Hall 102, San Francisco, CA 94158, jeremy.gordon@ucsf.edu, Phone: 415-476-9786.

Introduction

Hyperpolarized (HP) carbon-13 MR has been investigated in animals since 2006 to provide a unique window into cellular metabolism, enabling the quantification of enzyme-catalyzed conversion rates that inform on critical cellular biochemistry in both normal and pathologic conditions[1–3]. A first-in-human proof of concept clinical trial of HP [1-^{13}C]pyruvate completed in 2013 demonstrated feasibility and safety in patients[4]. The subsequent development of commercial research polarizers enabled new technical developments and initial human studies over the past 5 years in a variety of applications including prostate cancer, brain tumors, renal cancer, cardiac disease, pancreatic cancer, traumatic brain injury and breast cancer[5–14].

Since 2018, numerous studies have focused on investigating cerebral energy metabolism in the normal human brain and neuro-pathologies, demonstrating novel insights into brain bioenergetics by measuring HP pyruvate conversions to lactate and bicarbonate[6,10,11,15–17]. Conversion from pyruvate to lactate and to bicarbonate provides a measure of metabolic preference for either oxidative phosphorylation, which generates bicarbonate, or glycolytic metabolism, which generates lactate. The normal brain produces both lactate and bicarbonate, and increased lactate and decreased bicarbonate production were observed in brain tumor lesions[6,15]. These studies support the utility of HP pyruvate metabolism as a biomarker of brain tumor metabolic reprogramming and response to therapy.

Recent technical advances for HP studies have shown that metabolic quantification could be further improved through specialized acquisition and denoising techniques[18–21]. These techniques provide improved SNR and finer spatial resolution, enabling better localization of metabolism. In particular, a multi-resolution HP ^{13}C EPI approach was developed that enables the acquisition of the injected HP ^{13}C pyruvate at a higher spatial resolution than its metabolic products lactate and bicarbonate with their lower inherent SNR[18]. The purpose of this study was to apply for the first time this multi-resolution approach and specialized analysis to investigate HP pyruvate-to-lactate conversion rates, k_{PL}, in the normal brain with the motivation that higher pyruvate resolution could reduce partial volume effects of extracellular HP pyruvate in cerebral blood vessels that could cause errors in intracellular k_{PL} measurements.

Methods

HP brain studies were performed in six healthy human volunteer subjects with informed consent according to University of California San Francisco IRB and FDA IND approved protocols. The mean age of the subjects was 41.2 years (range 29–61 years) and all subjects were male. Before each study, a pharmacist prepared samples containing 1.47 g of Good Manufacturing Practice grade [1-^{13}C]pyruvic acid (MilliporeSigma Isotec) and 15 mM trityl electron paramagnetic agent (EPA; AH111501, GE Healthcare). The samples were polarized using a SPINlab polarizer (GE Healthcare) operating at 5 T and 0.8 K for > 2 hours. After dissolution of the polarized samples, the EPA was removed by filtration, the solution was neutralized with a Tris-buffered NaOH solution, and the quality control parameters of pH, pyruvate and residual EPA concentrations, polarization, and temperature were measured

prior to injection. In parallel, the sterile filter (0.2 μm, ZenPure, Manassas, VA) was tested in agreement with manufacturer specifications prior to injection. After release by a pharmacist, a 0.43 mL/kg dose of ~250 mM pyruvate was injected at a rate of 5 mL/s, followed by a 20 mL sterile saline flush (0.9% sodium chloride, Baxter Healthcare Corporation).

Studies were performed on a 3T MR scanner (MR750, GE Healthcare) using an integrated 8 channel ^{1}H/24 channel ^{13}C phased array receiver with an 8-rung low-pass ^{13}C volume transmit coil (Rapid Biomedical, Würzburg, Germany). Hyperpolarized ^{13}C data were acquired with a metabolite-selective imaging approach, using a singleband spectral-spatial RF pulse for excitation (passband FWHM = 130 Hz, stopband = 868 Hz) and a single-shot symmetric echoplanar readout for encoding[22]. Scan parameters were 125 ms TR, 30.7 ms TE, 32 × 32 matrix size, ±19.23 kHz BW, 1.064 ms echo-spacing, and eight slices with an axial orientation. Data acquisition started 5 seconds after the end of the saline injection for the first three subjects and immediately after the end of the saline injection for the latter three subjects. Pyruvate was excited with a 20° flip angle and lactate and bicarbonate were excited with a 30° flip angle. The slice thickness was 20 mm for the first subject and 15 mm for the other five subjects. The in-plane spatial resolution for each metabolite was changed by independently scaling the encoding gradients, resulting in 7.5 × 7.5 mm^2 resolution for pyruvate and 15 × 15 mm^2 resolution for lactate and bicarbonate. Twenty time points were acquired with a 3 second temporal resolution for a total scan time of one minute. Immediately following imaging, a non-localized spectrum was acquired to confirm the center frequency was set correctly. For anatomic reference, ^{1}H 3D inversion-recovery spoiled gradient-recalled echo (IR-SPGR) was acquired with the dual-tuned coil. ^{1}H 3D IR-SPGR scan parameters were 6.7 ms TR, 2.5 ms TE, 450 ms IR time, 25.6 × 25.6 × 18.6 cm^2 FOV, 256 × 256 × 124 matrix size (1 × 1 × 1.5 mm^3 resolution).

The ^{13}C EPI data were reconstructed using the Orchestra toolbox (GE Healthcare). Multichannel data were pre-whitened[23] and then coil combined using pyruvate to estimate the coil weights[24]. Denoising was performed on the coil-combined data using global-local higher-order singular value decomposition (GL-HOSVD) as described in Kim et al. for hyperpolarized MRI[20]. To quantify the reduction in partial volume effects with variable-resolution EPI, a synthetic 15 × 15 mm^2 pyruvate data set was obtained by cropping the central 16 × 16 region of k-space, zeropadding to the original matrix size (32 × 32), Fermi filtering to minimize Gibbs ringing, and transforming back to the image domain. Lactate and bicarbonate images were cropped and zeropadded to match the pyruvate FOV and matrix size, and signal values were normalized to voxel volume to account for the different acquisition resolution. Proton images were used in the FSL FAST algorithm[25] to generate brain masks, and the proton images were also summed in the slice dimension to match the carbon slice thickness.

Kinetic rate constants for each voxel were computed using an inputless two-site model to generate quantitative maps of pyruvate-to-lactate conversion (k_{PL})[26]. With the same lactate data, multi-resolution and constant-resolution k_{PL} maps were generated: one using the 7.5 × 7.5 mm^2 resolution pyruvate data and the other using the synthetic 15 × 15 mm^2 resolution pyruvate data. Kinetic rate maps were thresholded to select voxels that had a lactate area-under-curve (AUC) SNR > 5 and fitting error < 30%. Here we used the

fitting error as defined in Mammoli et al[26], where an absolute fitting error is defined to be half of the 95% confidence interval range from the nonlinear least squares fitting and the fitting error is the absolute error divided by the fitted rate constant. Due to limited k_{PB} coverage in white matter after SNR and fitting error thresholding, k_{PB} maps were not considered for this analysis. k_{PL} percent differences between the different resolutions were calculated by taking the difference of multi-resolution k_{PL} and constant-resolution k_{PL} and dividing by the constant-resolution k_{PL} on a voxel-wise basis. Lactate-to-pyruvate AUC ratios were also calculated using both pyruvate resolutions. To examine local kinetic rates across the six subjects for both resolution schemes, four voxels were manually selected in each study representing brain near arteries, brain near veins, white matter and gray matter. Statistical analysis with two-sided Wilcoxon signed rank tests was used to compare the paired multi-resolution and constant-resolution voxels.

Results

High resolution 7.5 × 7.5 mm^2 pyruvate images exhibit increased spatial delineation of brain structures and decreased partial volume effects compared to the coarse resolution 15 × 15 mm^2 pyruvate images as shown in Figure 1. In particular, high pyruvate signals from the gray matter, cerebral arteries, and sagittal sinus spill over into surrounding brain areas in the coarse resolution images. The lactate and bicarbonate images exhibit adequate SNR > 5 at 15 × 15 mm^2 resolution.

In this study, dynamic high resolution pyruvate images also improve identification of pyruvate arrival in cerebral blood vessels. In Figure 2 the pyruvate bolus is seen first in the internal carotid and middle cerebral arteries, followed by the transverse and sagittal sinuses after one 3-second time frame. The arterial pyruvate signal fades after 15 seconds, whereas the venous pyruvate signal is maintained for the duration of the 60-second acquisition.

The increased spatial delineation of high resolution pyruvate images is also apparent in the multi-resolution k_{PL} maps in Figure 3. The k_{PL} values were higher for multi-resolution kinetic maps, especially for the pons in the most inferior slice and white matter in the 3^{rd} and 4^{th} slices. The partial volume effect of decreased k_{PL} was most apparent near the ventricles and sagittal sinus, regions where high pyruvate signal spilled over from highly perfused gray matter and the sagittal sinus. Supporting Information Table S1 summarizes the mean and standard deviation (SD) of k_{PL} and lactate-to-pyruvate AUC ratios in the brain for each subject. Multi-resolution k_{PL} and AUC ratio means and SDs were significantly higher ($p < 0.05$) than constant-resolution k_{PL} and AUC ratio means and SDs. Average differences for multi-resolution as compared to constant-resolution were: 19% and 70% increase in k_{PL} mean and SD; 22% and 93% increase in AUC ratio mean and SD. For k_{PL} calculated from signals summed over the whole brain, the average percent k_{PL} difference across subjects was 3% higher for multi-resolution data than for constant-resolution data.

To compare k_{PL} between multi-resolution and constant-resolution datasets on a regional basis, we selected voxels in each subject near the arteries and veins, in addition to voxels in white and gray matter. Supporting Information Table S2 summarizes the k_{PL} values in the selected voxels for all subjects. Figure 4 shows the selected voxel positions in proton images

and k_{PL} maps for one subject. In this particular volunteer, multi-resolution k_{PL} values were 169, 65 and 44 percent higher than constant-resolution k_{PL} values for voxels near arteries, near veins and in white matter respectively. These k_{PL} differences are also present for the selected voxels in all subjects ($p < 0.05$), summarized in Table 1. The same effect of the multi-resolution approach is also observed for lactate-to-pyruvate AUC ratios, reported in Supporting Information S3. This difference in k_{PL} values and AUC ratios indicates that less extracellular pyruvate signal was present in the higher-resolution pyruvate voxels than in the coarse-resolution pyruvate voxels, since the lactate signal used for the multi-resolution and constant-resolution k_{PL} maps was identical.

Discussion

In this study, we utilized a multi-resolution acquisition to determine if higher pyruvate resolution could reduce the inclusion of extracellular pyruvate signals in blood vessels that is not metabolized like intracellular pyruvate in the brain and thus can cause errors in k_{PL} quantification. Higher spatial resolution for pyruvate (7.5×7.5 mm^2 versus 15×15 mm^2) decreased the partial volume spillover of vascular pyruvate signals into nearby brain voxels, and as a result the k_{PL} and lactate-to-pyruvate AUC ratios of those voxels calculated from multi-resolution data was higher than those calculated from constant-resolution data. Although the average k_{PL} difference between resolutions for the whole brain was only 3%, for voxels near cerebral arteries the average k_{PL} difference was up to 83%. This indicates that the partial volume effect of coarser resolution changes pyruvate signal magnitudes in a localized manner. Because of this localization, the magnitude of difference between resolutions is small when looking at the whole brain versus examining individual voxels. This partial volume effect was most apparent for voxels in white matter and voxels near cerebral arteries and veins. Using multi-resolution images for kinetic quantification provided more accurate k_{PL} and lactate-to-pyruvate AUC ratio estimates, especially near cerebral blood vessels with large amounts of pyruvate that are not available for metabolic conversion.

In addition, the multi-resolution acquisition scheme takes advantage of the high pyruvate SNR inherent to HP pyruvate studies by acquiring the injected substrate at higher resolution. These higher resolution pyruvate images improve the visualization of neuro-vascular structures and could potentially be used to extract perfusion-weighted information in addition to metabolic conversion[27]. The GL-HOSVD denoising also improves SNR for all metabolites[20], potentially enabling even further improvements in spatial resolution for future studies. Combining a multi-resolution acquisition with spatiotemporal denoising provides both high SNR and high spatial resolution, which in turn improves the accuracy of metabolic quantification.

In relation to previous HP studies on normal brain metabolism, this work studies the impact of multi-resolution acquisition on k_{PL} values and lactate-to-pyruvate AUC ratios. Prior studies have reported on the regional distribution of HP lactate production in terms of lactate-to-pyruvate AUC ratio, lactate z-score, and k_{PL}[16,17]. While there are multiple metrics that can be used to quantify HP data, using multi-resolution images improves k_{PL} and lactate-to-pyruvate AUC ratio metabolic quantification due to reduced partial volume effects. The multi-resolution EPI approach is also flexible, as the resolutions and flip angles can be

customized to each metabolite depending on SNR. Other metabolite-selective methods used for HP imaging such as spiral and balanced steady state free precession offer benefits in terms of speed and SNR and are also compatible with a multi-resolution imaging scheme.

Acquiring pyruvate with finer resolution allows for improved visualization of neurovascular structures and more accurate quantification of metabolite kinetics, but the multi-resolution acquisition comes with certain drawbacks. For this study, the metabolite signals were normalized to their respective voxel volumes for quantification. This method of matching the different resolutions assumes uniform signal distribution throughout voxels, which is not true for every voxel. Increasing the pyruvate resolution with a single-shot readout entails a longer readout time, which can lead to increased geometric distortion in regions of high B0 inhomogeneity. This could be ameliorated by incorporating a field map into the reconstruction or alternating the blip direction during the dynamic acquisition[28,29]. Limitations of this study also include the lack of in vivo constant-resolution data to directly compare to the acquired multi-resolution data. Previous studies with constant-resolution echoplanar and spiral trajectories used different echo times, which may affect the calculated kinetic rates due to differences in $T2^*$[30] and require a correction to directly compare with the values from this study. Despite the variation in acquisition delays employed across this study, the kinetic modeling of k_{PL} used did not require estimation of an input function and was therefore less sensitive to bolus arrival time, so long as the inflow of pyruvate was sufficiently captured[31]. The 0 second and 5 second delays both enabled sufficient pyruvate signal to be captured for the purposes of fitting.

Conclusions

Acquiring hyperpolarized ^{13}C pyruvate studies with a multi-resolution approach minimizes partial volume effects from vascular pyruvate signals while maintaining the SNR of downstream metabolites. Utilizing higher resolution pyruvate images for kinetic fitting reduced partial volume effects and increased the calculated kinetic rate values, particularly around the superior sagittal sinus and cerebral arteries where high pyruvate signals spill over from the large blood vessels. This hyperpolarized ^{13}C data showed that acquiring pyruvate with finer resolution improved the quantification of kinetic rates throughout the human brain.

Supplementary Material

Refer to Web version on PubMed Central for supplementary material.

Acknowledgements

This research was supported by NIH grants (PO1-CA118816, U01-EB026412, P41-EB013598) and the UCSF NICO project. Special thanks to the Aarhus University Magnetic Resonance Research Center for contributing to the data collection process.

References

1. Golman K, in ‘t Zandt R, Thaning M. Real-time metabolic imaging. Proceedings of the National Academy of Sciences. 2006;103(30):11270–11275. doi:10.1073/pnas.0601319103

2. Kurhanewicz J, Vigneron DB, Ardenkjaer-Larsen JH, et al. Hyperpolarized 13C MRI: Path to Clinical Translation in Oncology. Neoplasia. 2019;21(1):1–16. doi:10.1016/j.neo.2018.09.006 [PubMed: 30472500]
3. Wang ZJ, Ohliger MA, Larson PEZ, et al. Hyperpolarized ^{13}C MRI: State of the Art and Future Directions. Radiology. 2019;291(2):273–284. doi:10.1148/radiol.2019182391 [PubMed: 30835184]
4. Nelson SJ, Kurhanewicz J, Vigneron DB, et al. Metabolic Imaging of Patients with Prostate Cancer Using Hyperpolarized [1–13C]Pyruvate. Science Translational Medicine. 2013;5(198):198ra108–198ra108. doi:10.1126/scitranslmed.3006070
5. Apps A, Lau JYC, Miller JJJJ, et al. Proof-of-Principle Demonstration of Direct Metabolic Imaging Following Myocardial Infarction Using Hyperpolarized 13C CMR. JACC: Cardiovascular Imaging. 2021;14(6):1285–1288. doi:10.1016/j.jcmg.2020.12.023 [PubMed: 33582059]
6. Autry AW, Gordon JW, Chen HY, et al. Characterization of serial hyperpolarized 13C metabolic imaging in patients with glioma. NeuroImage: Clinical. 2020;27:102323. doi:10.1016/j.nicl.2020.102323 [PubMed: 32623139]
7. Crane JC, Gordon JW, Chen H, et al. Hyperpolarized ^{13}C MRI data acquisition and analysis in prostate and brain at University of California, San Francisco. NMR in Biomedicine. 2021;34(5). doi:10.1002/nbm.4280
8. Gallagher FA, Woitek R, McLean MA, et al. Imaging breast cancer using hyperpolarized carbon-13 MRI. Proc Natl Acad Sci USA. 2020;117(4):2092–2098. doi:10.1073/pnas.1913841117 [PubMed: 31964840]
9. Granlund KL, Tee SS, Vargas HA, et al. Hyperpolarized MRI of Human Prostate Cancer Reveals Increased Lactate with Tumor Grade Driven by Monocarboxylate Transporter 1. Cell Metabolism. 2020;31(1):105–114.e3. doi:10.1016/j.cmet.2019.08.024 [PubMed: 31564440]
10. Hackett EP, Pinho MC, Harrison CE, et al. Imaging Acute Metabolic Changes in Patients with Mild Traumatic Brain Injury Using Hyperpolarized [1–13C]Pyruvate. iScience. 2020;23(12):101885. doi:10.1016/j.isci.2020.101885 [PubMed: 33344923]
11. Miloushev VZ, Granlund KL, Boltyanskiy R, et al. Metabolic Imaging of the Human Brain with Hyperpolarized ^{13}C Pyruvate Demonstrates ^{13}C Lactate Production in Brain Tumor Patients. Cancer Res. 2018;78(14):3755–3760. doi:10.1158/0008-5472.CAN-18-0221 [PubMed: 29769199]
12. Stødkilde-Jørgensen H, Laustsen C, Hansen ESS, et al. Pilot Study Experiences With Hyperpolarized [1- ^{13}C]pyruvate MRI in Pancreatic Cancer Patients. J Magn Reson Imaging. 2020;51(3):961–963. doi:10.1002/jmri.26888 [PubMed: 31368215]
13. Tang S, Meng MV, Slater JB, et al. Metabolic imaging with hyperpolarized ^{13}C pyruvate magnetic resonance imaging in patients with renal tumors—Initial experience. Cancer. 2021;127(15):2693–2704. doi:10.1002/cncr.33554 [PubMed: 33844280]
14. Tran M, Latifoltojar A, Neves JB, et al. First-in-human *in vivo* non-invasive assessment of intra-tumoral metabolic heterogeneity in renal cell carcinoma. BJR|case reports. 2019;5(3):20190003. doi:10.1259/bjrcr.20190003
15. Park I, Larson PEZ, Gordon JW, et al. Development of methods and feasibility of using hyperpolarized carbon-13 imaging data for evaluating brain metabolism in patient studies: Hyperpolarized Carbon-13 Metabolic Imaging of Patients With Brain Tumors. Magn Reson Med. 2018;80(3):864–873. doi:10.1002/mrm.27077 [PubMed: 29322616]
16. Grist JT, McLean MA, Riemer F, et al. Quantifying normal human brain metabolism using hyperpolarized [1–13C]pyruvate and magnetic resonance imaging. NeuroImage. 2019;189:171–179. doi:10.1016/j.neuroimage.2019.01.027 [PubMed: 30639333]
17. Lee CY, Soliman H, Geraghty BJ, et al. Lactate topography of the human brain using hyperpolarized 13C-MRI. NeuroImage. 2020;204:116202. doi:10.1016/j.neuroimage.2019.116202 [PubMed: 31557546]
18. Gordon JW, Autry AW, Tang S, et al. A variable resolution approach for improved acquisition of hyperpolarized ^{13}C metabolic MRI. Magn Reson Med. 2020;84(6):2943–2952. doi:10.1002/mrm.28421 [PubMed: 32697867]
19. Chen H, Autry AW, Brender JR, et al. Tensor image enhancement and optimal multichannel receiver combination analyses for human hyperpolarized ^{13}C MRSI. Magn Reson Med. 2020;84(6):3351–3365. doi:10.1002/mrm.28328 [PubMed: 32501614]

20. Kim Y, Chen HY, Autry AW, et al. Denoising of hyperpolarized 13 C MR images of the human brain using patch-based higher-order singular value decomposition. Magn Reson Med. Published online June 25, 2021. doi:10.1002/mrm.28887
21. Ma J, Park JM. Super-Resolution Hyperpolarized 13C Imaging of Human Brain Using Patch-Based Algorithm. Tomography. 2020;6(4):343–355. doi:10.18383/j.tom.2020.00037 [PubMed: 33364424]
22. Gordon JW, Chen HY, Autry A, et al. Translation of Carbon-13 EPI for hyperpolarized MR molecular imaging of prostate and brain cancer patients. Magn Reson Med. 2019;81(4):2702–2709. doi:10.1002/mrm.27549 [PubMed: 30375043]
23. Pruessmann KP, Weiger M, Börnert P, Boesiger P. Advances in sensitivity encoding with arbitrary k-space trajectories. Magn Reson Med. 2001;46(4):638–651. doi:10.1002/mrm.1241 [PubMed: 11590639]
24. Zhu Z, Zhu X, Ohliger MA, et al. Coil combination methods for multi-channel hyperpolarized 13C imaging data from human studies. Journal of Magnetic Resonance. 2019;301:73–79. doi:10.1016/j.jmr.2019.01.015 [PubMed: 30851668]
25. Zhang Y, Brady M, Smith S. Segmentation of brain MR images through a hidden Markov random field model and the expectation-maximization algorithm. IEEE Trans Med Imaging. 2001;20(1):45–57. doi:10.1109/42.906424 [PubMed: 11293691]
26. Mammoli D, Gordon J, Autry A, et al. Kinetic Modeling of Hyperpolarized Carbon-13 Pyruvate Metabolism in the Human Brain. IEEE Trans Med Imaging. 2020;39(2):320–327. doi:10.1109/TMI.2019.2926437 [PubMed: 31283497]
27. Park I, Lupo JM, Nelson SJ. Correlation of Tumor Perfusion Between Carbon-13 Imaging with Hyperpolarized Pyruvate and Dynamic Susceptibility Contrast MRI in Pre-Clinical Model of Glioblastoma. Mol Imaging Biol. 2019;21(4):626–632. doi:10.1007/s11307-018-1275-y [PubMed: 30225760]
28. Jezzard P, Balaban RS. Correction for geometric distortion in echo planar images from B0 field variations. Magnetic Resonance in Medicine. 1995;34(1):65–73. doi:10.1002/mrm.1910340111 [PubMed: 7674900]
29. Miller JJ, Lau AZ, Tyler DJ. Susceptibility-induced distortion correction in hyperpolarized echo planar imaging. Magnetic Resonance in Medicine. 2018;79(4):2135–2141. doi:10.1002/mrm.26839 [PubMed: 28722201]
30. Chen HY, Gordon JW, Bok RA, et al. Pulse sequence considerations for quantification of pyruvate-to-lactate conversion k_{PL} in hyperpolarized ^{13}C imaging. NMR in Biomedicine. 2019;32(3):e4052. doi:10.1002/nbm.4052 [PubMed: 30664305]
31. Larson PEZ, Chen H, Gordon JW, et al. Investigation of analysis methods for hyperpolarized 13C-pyruvate metabolic MRI in prostate cancer patients. NMR in Biomedicine. 2018;31(11). doi:10.1002/nbm.3997

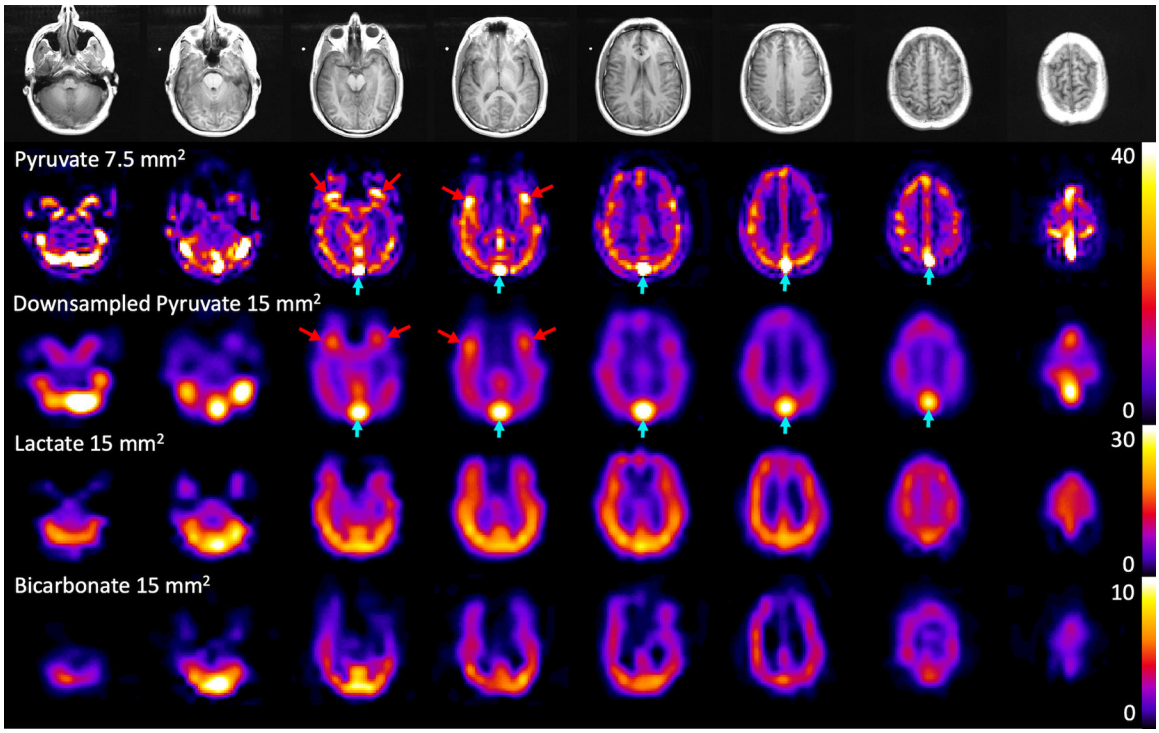

Figure 1.

Hyperpolarized ^{13}C pyruvate, lactate and bicarbonate signals summed over 60 seconds with reference proton images of subject 2. The 15 × 15 mm^2 pyruvate data set was obtained by cropping 7.5 × 7.5 mm^2 pyruvate k-space data, zerofilling, and applying a Fermi filter. The downsampled pyruvate images exhibited partial volume spillover of signal particularly in the vasculature, including the middle cerebral arteries indicated by red arrows in slices 3–4 and the superior sagittal sinus indicated by blue arrows in slices 3–7. Carbon images were zerofilled once for display and intensity units are arbitrary.

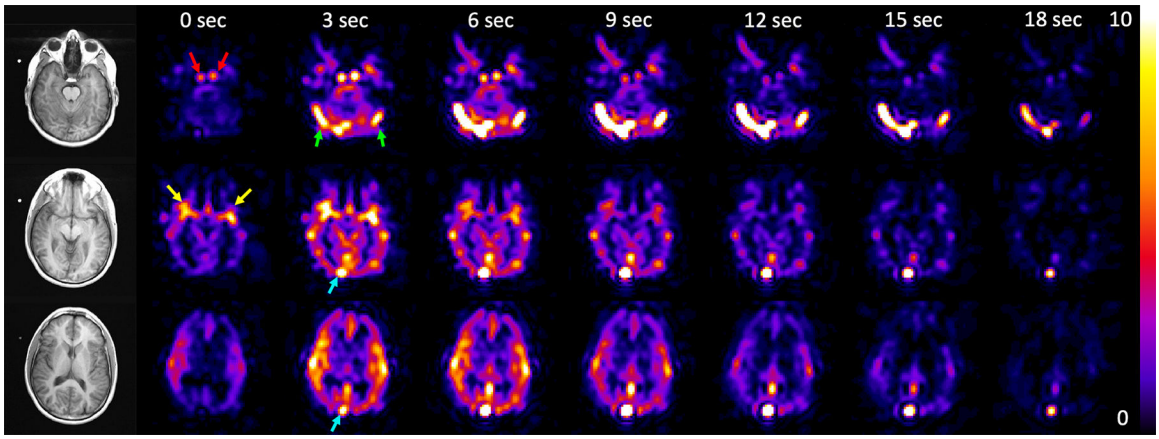

Figure 2.

Hyperpolarized ^{13}C pyruvate dynamic images of pyruvate delivery in the brain with reference proton images of subject 5. The colored arrows point out arrival of pyruvate in the anterior cerebral circulation (internal carotid, *red*; middle cerebral arteries, *yellow*) and transit into the superior sagittal (*blue*) and transverse dural venous sinuses (*green*). The arterial pyruvate signal disappears approximately 15 seconds after arrival, while the venous pyruvate signal remains high and visible towards the end of the acquisition. Carbon images were zerofilled once for display and intensity units are arbitrary.

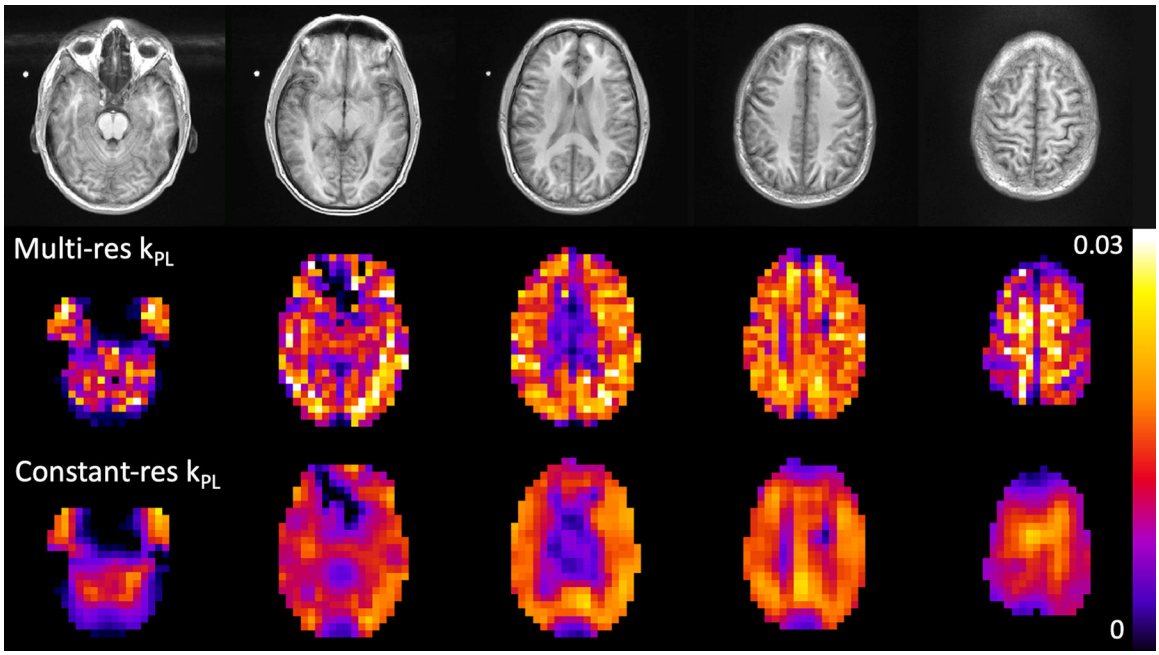

Figure 3.

Kinetic rate maps for pyruvate-to-lactate conversion (k_{PL}, s^{-1}) in subject 1, using 15 × 15 mm^2 lactate signals with 7.5 × 7.5 mm^2 pyruvate (multi-resolution) and synthetic 15 × 15 mm^2 pyruvate (constant-resolution) brain-masked images, along with reference proton images. The constant-resolution k_{PL} map showed smoothing and loss of fine detail of the kinetic rates in the brain as compared to the multi-resolution k_{PL} map.

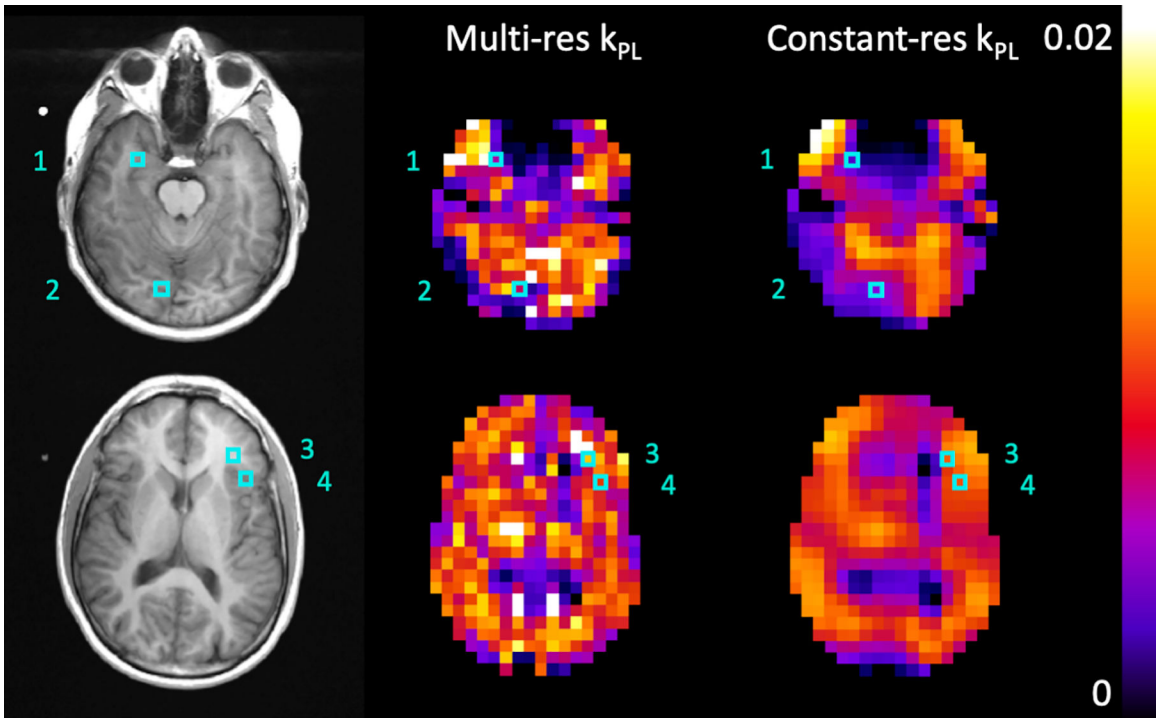

Figure 4.

Kinetic rate maps for pyruvate-to-lactate conversion (k_{PL}, s^{-1}) for subject 5 with four selected voxel positions shown in multi-resolution and constant-resolution maps. The voxels numbered 1–4 refer to locations near artery, near vein, in white matter, and in gray matter respectively. Voxels near arteries, veins and in white matter exhibited 169, 65, and 44 percent higher k_{PL} for multi-resolution maps respectively, indicating less pyruvate signal contributions from blood vessels. The voxel in gray matter showed 7 percent k_{PL} decrease for multi-resolution, indicating less change in the regional pyruvate signal between higher and coarser resolutions.

Table 1.

Summary of percent differences in pyruvate-to-lactate conversion (k_{PL}) between multi-resolution and constant-resolution data from six subjects. Single voxels near arteries, veins, in white matter, and in gray matter were selected manually. Multi-resolution k_{PL} was significantly higher for voxels near arteries and veins and voxels in white matter ($p < 0.05$), showing a decrease in partial volume spillover of vascular pyruvate. There were inconsistent differences for gray matter voxels. Subject 4 values were an average of two hyperpolarized C^{13} pyruvate injections in the same exam and stars indicate statistical significance ($p < 0.05$).

Subject	Near Artery % k_{PL} Difference	Near Vein % k_{PL} Difference	White Matter % k_{PL} Difference	Gray Matter % k_{PL} Difference
1	52	77	47	1
2	57	96	75	46
3	37	106	57	51
4	32	73	27	−16
5	169	65	44	−7
6	153	30	71	−12
Mean ± SD	83 ± 61*	75 ± 27*	54 ± 18*	10 ± 30